University of Groningen

Extremely efficient terahertz high-harmonic generation in graphene by hot Dirac fermions

Hafez, Hassan A.; Kovalev, Sergey; Deinert, Jan-Christoph; Mics, Zoltan; Green, Bertram; Awari, Nilesh; Chen, Min; Germanskiy, Semyon; Lehnert, Ulf; Teichert, Jochen

IMPORTANT NOTE: You are advised to consult the publisher's version (publisher's PDF) if you wish to cite from it. Please check the document version below.

Document Version
Publisher's PDF, also known as Version of record

Publication date:
2018

[Link to publication in University of Groningen/UMCG research database](#)

LETTER

Extremely efficient terahertz high–harmonic generation in graphene by hot Dirac fermions

Hassan A. Hafez[1,2,3,7], Sergey Kovalev[4,7], Jan–Christoph Deinert[4], Zoltán Mics[2], Bertram Green[4], Nilesh Awari[4,5], Min Chen[4], Semyon Germanskiy[4], Ulf Lehnert[4], Jochen Teichert[4], Zhe Wang[4], Klaas–Jan Tielrooij[6], Zhaoyang Liu[2], Zongping Chen[2], Akimitsu Narita[2], Klaus Müllen[2], Mischa Bonn[2], Michael Gensch[4]* & Dmitry Turchinovich[1,2]*

Multiple optical harmonic generation—the multiplication of photon energy as a result of nonlinear interaction between light and matter—is a key technology in modern electronics and optoelectronics, because it allows the conversion of optical or electronic signals into signals with much higher frequency, and the generation of frequency combs. Owing to the unique electronic band structure of graphene, which features massless Dirac fermions[1–3], it has been repeatedly predicted that optical harmonic generation in graphene should be particularly efficient at the technologically important terahertz frequencies[4–6]. However, these predictions have yet to be confirmed experimentally under technologically relevant operation conditions. Here we report the generation of terahertz harmonics up to the seventh order in single-layer graphene at room temperature and under ambient conditions, driven by terahertz fields of only tens of kilovolts per centimetre, and with field conversion efficiencies in excess of 10^{-3}, 10^{-4} and 10^{-5} for the third, fifth and seventh terahertz harmonics, respectively. These conversion efficiencies are remarkably high, given that the electromagnetic interaction occurs in a single atomic layer. The key to such extremely efficient generation of terahertz high harmonics in graphene is the collective thermal response of its background Dirac electrons to the driving terahertz fields. The terahertz harmonics, generated via hot Dirac fermion dynamics, were observed directly in the time domain as electromagnetic field oscillations at these newly synthesized higher frequencies. The effective nonlinear optical coefficients of graphene for the third, fifth and seventh harmonics exceed the respective nonlinear coefficients of typical solids by 7–18 orders of magnitude[7–9]. Our results provide a direct pathway to highly efficient terahertz frequency synthesis using the present generation of graphene electronics, which operate at much lower fundamental frequencies of only a few hundreds of gigahertz.

Great demand exists in the field of modern ultrahigh-speed electronics for efficient active functional materials supporting very high, terahertz (10^{12} Hz, THz), frequencies. Since the advent of graphene, several theoretical proposals (see, for example, refs [4–6]) have predicted efficient THz frequency multiplication or harmonic generation in single-layer graphene in realistic technologically relevant scenarios, including room-temperature operation. Despite considerable efforts, the experimental verification of these predictions has so far not been achieved. Signatures of THz harmonics have recently been demonstrated[10] in a near-intrinsic epitaxial 45-layer graphene sample, but these were observable only at a cryogenic temperature. The nonlinearity mechanism in ref. [10] critically relies on inter-band THz transitions in graphene, which at a room temperature are essentially Pauli-blocked. Further, it was recently suggested that efficient THz harmonic generation in graphene is unfeasible[11] owing to the ultrafast relaxation of THz-excited electrons and holes, prohibiting coherent electronic response to driving THz fields, which is typically required for the generation of THz or optical harmonics in other solids[12,13]. Consequently, it was

proposed to move away from the THz range to much higher infrared optical frequencies, where the generation of multiple optical harmonics was successfully demonstrated[11] in single-layer graphene under intense optical excitation, with peak electric field strengths reaching tens of megavolts per centimetre.

Here we show that the THz high-harmonic generation in single-layer graphene under realistic technological conditions is, in fact, an extremely efficient process, and that the THz nonlinearity of this atomically thin material greatly surpasses that of other solids. We demonstrate THz harmonic generation up to the seventh order in single-layer graphene at room temperature and under ambient conditions, using THz electric fields as weak as tens of kilovolts per centimetre, which is about three orders of magnitude lower (corresponding to peak powers one million times smaller) than that required for the observation of infrared-driven nonlinearity[11].

Previous experiments on the generation of optical harmonics in graphene critically relied on interband transitions in graphene in strong applied fields[10,11]. Here we show that the key to highly efficient THz harmonic generation in graphene is the introduction of the free background electron population, responding collectively to the driving THz field. These free background Dirac electrons, which can be easily introduced by the substrate or atmospheric doping, or by electronic gating, serve as an extremely efficient, yet highly nonlinear, intermediary energy reservoir: they facilitate and also strongly modulate the energy transfer between the THz field and graphene through a nonlinear intraband conductivity mechanism. Our experimental observations are fully reproduced by a model describing such energy transfer dynamics and the concurrent THz electromagnetic response of graphene.

Our sample is a typical monolayer graphene grown by chemical vapour deposition (CVD), deposited on a fused SiO_2 substrate (see ref. [14] and references therein). Basic characterization of the sample yielded a background free-carrier concentration of $N_c = 2.1 \times 10^{12}$ cm^{-2} and Fermi level of $E_F = 170$ meV at room temperature (see Methods and Extended Data Fig. 11).

Our experiment, schematically represented in Fig. 1a, was specifically designed for the observation of the THz harmonics in graphene in the time domain (see Methods and Extended Data Fig. 1). It was enabled by the use of TELBE, a new superconducting radiofrequency accelerator-based superradiant THz source[15]. Our measurements were performed at a repetition rate of 100 kHz and with linearly polarized THz electric fields incident normally on graphene. Narrow-band, multi-cycle quasi-monochromatic THz radiation pulses from TELBE (see Extended Data Fig. 2), with controllable peak field strength in the range of $E_f = 12$–85 kV cm^{-1} (where the subscript f indicates fundamental frequency) and full-width at half-maximum (FWHM) bandwidth below 70 GHz, were transmitted through the single-layer graphene deposited on a SiO_2 substrate and were detected in the time-domain as THz light-wave oscillations (see Methods and Extended Data Fig. 1). The THz transmission through a nominally

[1]Fakultät für Physik, Universität Duisburg-Essen, Duisburg, Germany. [2]Max Planck Institute for Polymer Research, Mainz, Germany. [3]Physics Department, Faculty of Science, Helwan University, Cairo, Egypt. [4]Helmholtz-Zentrum Dresden-Rossendorf, Dresden, Germany. [5]University of Groningen, Groningen, The Netherlands. [6]ICFO—Institut de Ciencies Fotoniques, The Barcelona Institute of Science and Technology, Barcelona, Spain. [7]These authors contributed equally: Hassan A. Hafez, Sergey Kovalev. *e-mail: m.gensch@hzdr.de; dmitry.turchinovich@uni-due.de
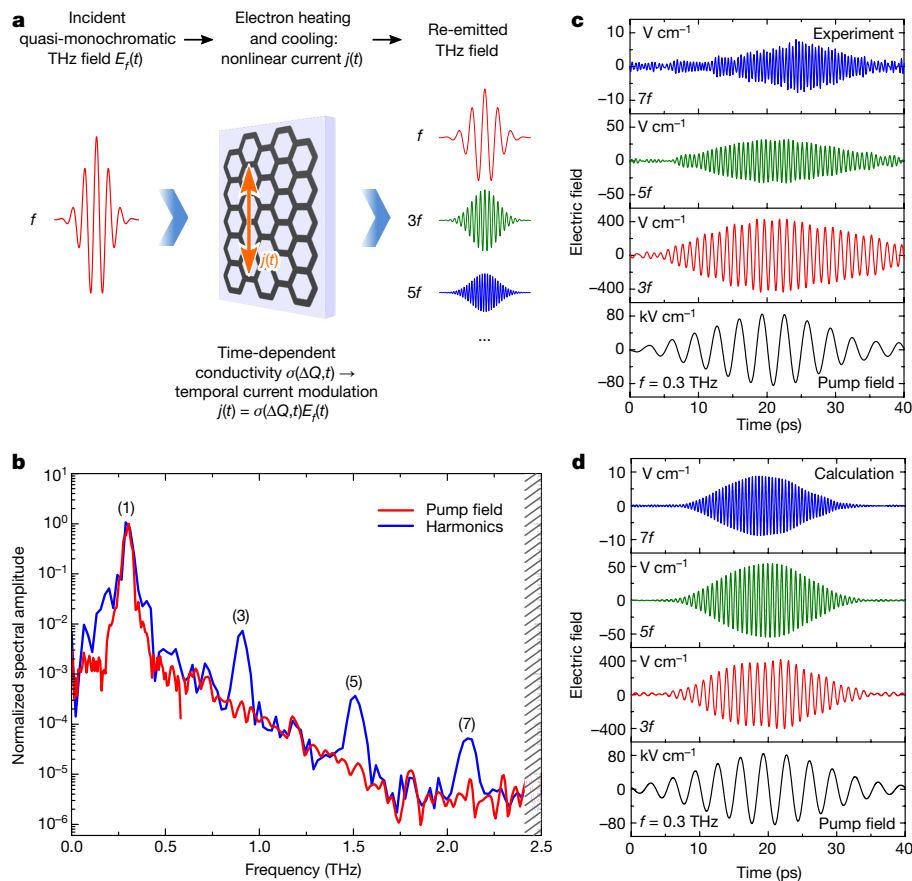
Fig. 1 | Schematic and main results of the THz high-harmonic generation. a, Schematic of the experiment: quasi-monochromatic, linearly polarized THz pump wave from the TELBE source is incident on a graphene sample, single-layer CVD-grown graphene deposited on SiO_2 substrate. The graphene has a Fermi level of $E_F = 170$ meV, free carrier density of $N_c = 2.1 \times 10^{12}$ cm^{-2} and electron momentum scattering time of $\tau = 47$ fs (all parameters correspond to full thermal equilibrium at 300 K). The peak electric field strength of the pump THz signal is controlled in the range 12–85 kV cm^{-1}, and the central frequency is varied in the range 0.3–0.68 THz. The incident THz field drives the nonlinear current in graphene, leading to re-emission at higher odd-order harmonics that appear in the spectrum of the transmitted THz signal. The THz fields are detected in the time domain directly as oscillations of electric field, using free-space electro-optic sampling with the cut-off frequency at 2.4 THz. All the experiments are carried out at room temperature and under ambient conditions. Q, electronic heat. **b,** Red line, amplitude spectrum of the incident pump THz wave at the fundamental frequency $f = 0.3$ THz with peak field strength $E_f = 85$ kV cm^{-1}, determined in the reference measurement. Blue line, the spectrum of the same THz wave transmitted through graphene on a substrate, with clearly visible generated harmonics of third, fifth and seventh order. The shaded area represents the detector cut-off. **c,** Pump wave (black line) and generated third, fifth and seventh THz harmonics for the case in **b**. The individual higher harmonics were Fourier-filtered from the complete nonlinear signal containing all the generated harmonics at once. **d,** Thermodynamic model calculation, corresponding to the measurements in **b** and **c**, using as input the experimental fundamental pump wave at frequency $f = 0.3$ THz (black line) and the basic parameters of graphene in full thermal equilibrium at 300 K.

identical bare SiO_2 substrate served as a reference, which exhibited no sign of THz nonlinearity. The cut-off frequency of our detector was 2.4 THz. All measurements were carried out at room temperature.

In Fig. 1b, c we show the typical results of our experiments. In Fig. 1b we show the amplitude spectra of the pump THz wave with a fundamental frequency of $f = 0.3$ THz and a peak electric field strength of $E_f = 85$ kV cm^{-1}, transmitted through the bare SiO_2 substrate (red line), and transmitted through the single-layer graphene on the SiO_2 substrate (blue line). Multiple THz harmonics up to the seventh order are clearly visible in the spectrum of the THz signal after interaction with graphene, with a pump-to-harmonic field conversion efficiency in excess of 10^{-3}, 10^{-4} and 10^{-5} for the third, fifth and seventh THz harmonics, respectively. Such nonlinear conversion efficiencies, especially observed at THz frequencies, are remarkable, given that the electromagnetic interaction occurs here within just one atomic layer. In Fig. 1c we demonstrate the measured THz harmonics directly in the time domain. Figure 1d shows the results of calculations based on the thermodynamic model of THz nonlinearity in graphene[14], using the experimental THz pump wave at fundamental frequency $f = 0.3$ THz as an input. The calculations in Fig. 1d capture all the key experimental

features in Fig. 1c, including the peak field strength in the generated harmonics, as well as the temporal shortening of the harmonic pulses with the increase in harmonic order. The essentials of our parameter-free model[14] are explained below, and the specific calculation details are provided in the Methods.

The underlying physical mechanism of THz harmonic generation in graphene is the creation of nonlinear electrical currents resulting from the strongly nonlinear intraband THz conductivity of graphene background electrons. In electronic thermal equilibrium, the intraband conductivity of graphene σ is determined by the concentration N_c and the temperature T_e of its background electronic population. For the intraband THz excitation of graphene, N_c is constant and the conductivity σ is thus governed by T_e. If graphene is sufficiently doped, so that $|E_F| > k_B T_e$, the rise in the electronic temperature leads to a reduction of conductivity[14,16–18] (here k_B is the Boltzmann constant). The application of THz electric field E to graphene leads to generation of a THz current $j = \sigma E$, and hence to deposition of energy into the electronic population (the power absorption coefficient of a material is directly proportional to its conductivity). One of the remarkable features of Dirac electrons in graphene is their ability to thermalize internally—that is, exchange
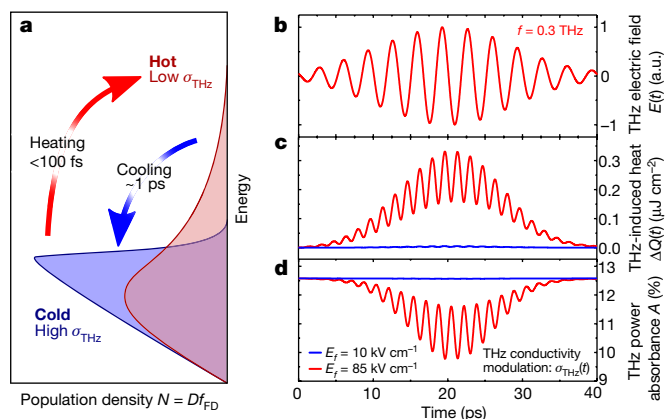
Fig. 2 | Illustration of the mechanism of THz harmonic generation in graphene, based on calculations with the thermodynamic model of intraband nonlinear THz conductivity of graphene. a–d, Temporal asymmetry of electron heating and cooling rates in graphene (**a**) leads to a situation where the application of a THz driving field (**b**) to the graphene electron population results in electronic heat accumulation $\Delta Q(t)$ (**c**) and hence in the temporal modulation (**d**) of the THz absorbance $A(t)$ and of the conductivity of graphene $\sigma(t)$. In these calculations the driving field (**b**) oscillates at the fundamental frequency $f = 0.3$ THz. Blue and red lines in **c** and **d** correspond to driving field peak amplitudes of 10 kV cm^{-1} and 85 kV cm^{-1}, respectively. The field strength of 10 kV cm^{-1} represents the regime of small-signal nonlinearity (no substantial modification of the sample properties on the timescale of the interaction with the THz wave), whereas the field strength of 85 kV cm^{-1} leads to considerable electron heating and thus to a substantial decrease in the absorption of graphene at the peak of interaction.

their kinetic energy and establish a common electronic temperature within the entire background electron population—on an ultrafast timescale below 100 femtoseconds[14,19–24], which is quasi-instantaneous as compared with the picosecond period of the THz field oscillation. Therefore, through such an ultrafast internal electronic thermalization, the excess energy deposited into graphene background electrons by the THz current is quasi-instantaneously converted into collective kinetic energy of the entire background electron population, that is into electronic heat, leading to a rise in T_e and to a concomitant decrease of σ. As a result of these interdependencies, the THz conductivity of graphene depends strongly nonlinearly on the driving THz field[14,17,25,26]: the stronger the field, the smaller the conductivity becomes.

The subsequent energy relaxation (cooling) of the hot electron population in graphene occurs through phonon emission on a timescale of a few picoseconds (see, for example, refs [20,25])—that is, with THz rate (see Methods). This phonon emission completes the energy conversion process in the THz excitation of graphene, in which the background population of Dirac electrons serves as a nonlinear intermediary in the transfer of energy from the absorbed THz field to the lattice of graphene.

The processes of heating and cooling of background Dirac electron population, leading to the reduction and recovery of the intraband THz conductivity in graphene, respectively, are schematically shown in Fig. 2a. Here $N(E) = D(E)f_{FD}(E,T)$ is the energy-dependent population density function for graphene background electrons, a product of the density of states D and the Fermi–Dirac distribution f_{FD}. Now we arrive at a situation in which the THz conductivity of graphene is not only nonlinear with the driving THz field (as facilitated by the direct conversion of absorbed THz energy into electronic heat) but also exhibits THz-rate recovery dynamics provided by the electron cooling rate (transfer of electronic heat to the lattice). The double interplay of quasi-instantaneous electron heating and THz-rate electron cooling in THz-driven graphene leads to highly nonlinear temporal modulation of the THz absorption in graphene, and hence of the THz conductivity, as illustrated in the calculations shown in Fig. 2b–d (see Methods for details). Consequently, a nonlinear current modulated by nonlinear

time-dependent conductivity is generated in graphene in response to the driving THz field $E(t)$. In the case of a monochromatic THz driving field $E_f(t)$ oscillating at a frequency f, the resulting nonlinear current in graphene, given its centrosymmetry, will contain contributions at odd-order harmonics f, $3f$, $5f$, $7f$, …, thus leading to electromagnetic re-emission at these harmonic frequencies (as illustrated schematically in Fig. 1a) and resulting in the appearance of these harmonics in the spectrum of the transmitted THz signal. In a centrosymmetric medium, the even-order harmonics cancel out, and thus cannot be generated[7]. Using the above thermodynamic model[14], the nonlinear propagation of THz signals through graphene can be readily calculated, only using experimentally determined parameters as input: the incident THz waveform at the fundamental frequency f; the conductivity parameters of the graphene sample measured in the linear regime in full thermal equilibrium at $T = 300$ K; the quasi-instantaneous electron heating (see discussion above and refs [19–24]); and picosecond-timescale cooling through phonon emission as measured in ref. [20]. We also note that no adjustable parameters are used in our model (see Methods).

Now we determine the harmonic generation efficiency and estimate the effective THz nonlinear optical susceptibility of graphene from the analysis of experimentally measured time-domain THz signals, such as those shown in Fig. 1c. In Fig. 3a, we show the dependency of the amplitude of the generated harmonics fields on that of the driving field. Here, to increase the dynamic range in the characterization of the third and fifth harmonic generation processes, our THz detection scheme was optimized to detect the harmonic signal only in the spectral window around 2 THz, whereas the driving fundamental frequency f of the THz source was varied as follows: $f = 0.68$ THz was used to generate the third harmonic at $3f = 2.04$ THz; $f = 0.37$ THz was used to generate the fifth harmonic at $5f = 1.85$ THz; and $f = 0.3$ THz was used to generate the seventh harmonic at $7f = 2.1$ THz. Depending on the order of the generated harmonic, the peak harmonic field strength was in the range 3–111 V cm^{-1}, whereas the pumping field strength was varied in the range 12–85 kV cm^{-1}. The efficiency parameters of the THz harmonic generation in this work are summarized in Table 1.

In the same Fig. 3a, as black solid lines, we present the results of the calculated pump-to-harmonic conversion efficiencies, using the parameter-free thermodynamic model[14] as explained above. The agreement between the experimental data and the parameter-free calculation is quantitative. The harmonic generation efficiency, shown in Fig. 3a, saturates with the pump field increase, as caused by the dissipative nature of the interaction between the THz field and the graphene electrons. In Fig. 2c, d we show the calculated temporal evolution of the THz field-induced electronic heat $\Delta Q(t)$ and the instantaneous THz power absorbance $A(t)$ of our graphene sample, driven by the THz field at the fundamental frequency $f = 0.3$ THz shown in Fig. 2b, and with the field strength at the lower and upper limits of our experiment: 10 kV cm^{-1} and 85 kV cm^{-1}, respectively. At the weaker driving field of 10 kV cm^{-1}, the evolution of both $\Delta Q(t)$ and $A(t)$ is very small. Here, the nonlinear interaction conditions between the THz field and graphene remain approximately constant over the entire interaction period, thus manifesting the small-signal nonlinearity regime. On the other hand, as the driving THz field increases by about an order of magnitude to 85 kV cm^{-1}, the effect of the THz field on the electronic system of graphene becomes very strong. At the peak of the interaction, the electronic heat $\Delta Q(t)$ reaches the value of 0.33 μJ cm^{-2}, leading to a reduction of the THz power absorbance of graphene by approximately 25%. This considerable absorption saturation naturally limits the energy transfer rate from the driving THz field to the electronic system, subsequently leading to the observed saturable behaviour of THz nonlinearity in graphene. The marked difference between the conditions of THz–graphene interaction for the cases of $E_f = 10$ kV cm^{-1} and $E_f = 85$ kV cm^{-1} in Fig. 2c, d illustrates the extremely nonlinear nature of the thermodynamic response of the Dirac electrons in graphene to the THz fields.

Importantly, at lower driving fields below approximately 20 kV cm^{-1}, both the data and the calculation of harmonic generation efficiency
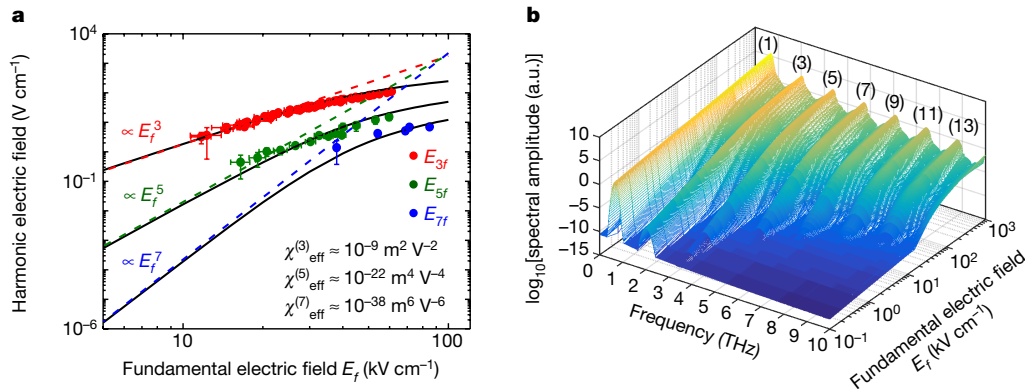
Fig. 3 | Efficiency of THz high-harmonic generation. a, Dependence of the generated harmonic field strength on the fundamental pump field strength. For the third, fifth and seventh harmonics, the fundamental field frequency was $f = 0.68$ THz, $f = 0.37$ THz and $f = 0.3$ THz, respectively, leading to corresponding higher harmonics of $3f = 2.04$ THz, $5f = 1.85$ THz and $7f = 2.1$ THz, respectively. Symbols represent data; black lines, parameter-free calculations using the thermodynamic model; dashed lines, power of 3 (red), power of 5 (green) and power of 7 (blue) fits corresponding to the small-signal nonlinearity regime below the driving field of about 20 kV cm^{-1}, which allows estimation of the third-, fifth- and seventh-order THz effective nonlinear susceptibilities of graphene, $\chi^{(3)}_{eff}$, $\chi^{(5)}_{eff}$ and $\chi^{(7)}_{eff}$, as indicated in the figure. The error bars for the pump fields are defined by the width of the chosen pulse intensity distribution. The error bars for the harmonic fields are derived from the sum of the standard deviations from multiple measurements and the background noise. **b**, Calculation of higher-order harmonic generation in graphene using the thermodynamic mechanism: amplitude spectra of the THz field transmitted through the graphene sample. The calculation was performed with sample parameters as used in this work ($N_c = 2.1 \times 10^{12}$ cm^{-2} and $E_F = 170$ meV), using the model incident THz field at $f = 0.68$ THz with peak strength in the range of 100 V cm^{-1} to 1 MV cm^{-1}. Harmonics up to 13th order appear in the spectrum within the 10^6 dynamic range with respect to the transmitted fundamental.

in Fig. 3a reduce to the phenomenological power-law dependencies $E_{mf} \propto E_f^m$, where m is the harmonic order (see dashed lines in Fig. 3a), manifesting the small-signal nonlinearity regime. In this regime, the nonlinear conversion can be described within the framework of effective odd-order nonlinear optical coefficients $\chi^{(m)}_{eff}$, precisely as expected for the nonlinear response in a centrosymmetric medium. From the purely power-law fits to the field conversion efficiencies (dashed lines in Fig. 3a), we determine the effective THz third-, fifth- and seventh-order nonlinear coefficients of graphene as $\chi^{(3)}_{eff} \approx 10^{-9}$ m^2 V^{-2}, $\chi^{(5)}_{eff} \approx 10^{-22}$ m^4 V^{-4} and $\chi^{(7)}_{eff} \approx 10^{-38}$ m^6 V^{-6}, respectively (see Methods for details). These values of THz nonlinear optical coefficients of graphene, determined by us at room temperature and under ambient conditions in a conventional CVD-grown single-layer graphene, exceed the corresponding nonlinearities of a typical solid by 7–18 orders of magnitude[7–9]. The third-order nonlinearity obtained in this work exceeds the corresponding values measured in single-layer graphene in the optical spectral range by 6–10 orders of magnitude[27–29] (we note, however, that the theoretical prediction of stronger optical-range response exists in the literature[30]); and the value reported in the infrared for the 50-layer graphene sample under cryogenic conditions and in strong magnetic field by at least one order of magnitude[31]. The fifth- and seventh-order THz nonlinear coefficients of graphene have not previously been reported in the literature, to the best of our knowledge.

We note here that the thermodynamic model of graphene conductivity does not contain any a priori defined effective nonlinear-optical coefficients of graphene, but rather describes the temporal evolution of the THz field-induced electronic heat and, hence, the instantaneous conductivity of graphene during its interaction with the incident THz electromagnetic wave of arbitrary shape. Very good agreement between our parameter-free calculation and the entirety of our data lends credence to our interpretation of the nature of the observed THz harmonic generation in graphene.

We estimate the limits of applicability of the purely thermodynamic picture of nonlinear THz response in doped graphene as the onset of coherent Bloch oscillations (see, for example, ref. [13]), which in graphene will occur at a pump field strength of 1–10 MV cm^{-1} (see Methods). We now illustrate the potential for higher-order THz harmonic generation in graphene using the thermodynamic mechanism, for typical experimental and technological scenarios. With the same material parameters of graphene as used in this work, we apply a model quasi-monochromatic waveform at fundamental $f = 0.68$ THz with varying peak field strengths in the range 100 V cm^{-1} to 1 MV cm^{-1}. This range comprises the linear regime of THz fields (of the order of a few kV cm^{-1}) and the regime of typical high-speed transistor channel fields (of the order of 100 kV cm^{-1})[32], and extends to the TELBE operation regime under projected design parameters of 1 MV cm^{-1} (ref. [15]). In Fig. 3b we show the corresponding calculated amplitude spectra of the transmitted THz waveform as a function of the peak electric field strength of the incident fundamental wave. As the driving electric field strength increases, higher-order harmonics keep appearing in the spectrum, with the 13th harmonic falling within the 10^6 dynamic range with respect to the transmitted fundamental, at a field strength for the driving signal of 1 MV cm^{-1}.

The very high THz nonlinear coefficients of graphene, measured in this work, suggest straightforward applications in ultrahigh-frequency (opto-)electronics. A driving electric field of tens of kilovolts per centimetre, as used here, is about one order of magnitude smaller than the typical channel field in ultra-high speed transistors[32]. Therefore, our results provide a direct pathway to purely electronic THz frequency synthesis within the present generation of graphene transistors operating at fundamental frequencies of a few hundred gigahertz[32]. Further, the observed nonlinear THz response of a single layer graphene can be made scalable, for example, by creating stratified structures with graphene-coated interfaces, or graphene-loaded waveguides or cavities.

Table 1 | Harmonic generation efficiencies and nonlinear coefficients of graphene

Generated harmonic order, m	Range of pump field strength, E_f (kV cm^{-1})	Range of harmonic field strength, E_{mf} (V cm^{-1})	Maximum field conversion efficiency, E_{mf}/E_f	Effective nonlinear coefficient, $\chi^{(m)}_{eff}$
3	12–61	3–111	2×10^{-3}	~10^{-9} m^2 V^{-2}
5	17–60	0.4–15	2.5×10^{-4}	~10^{-22} m^4 V^{-4}
7	38–85	1–7	8×10^{-5}	~10^{-38} m^6 V^{-6}

Ranges of pump and harmonic peak electric field strength, maximum field conversion efficiency and the THz nonlinear coefficients of graphene of third, fifth and seventh orders, established in the small-signal nonlinearity regime, are shown.

Finally, we note that our results on efficient THz harmonic generation in graphene by hot Dirac fermions could be potentially generalized to other representatives of the new class of Dirac materials, such as topological insulators, or Weyl and Dirac semimetals[33].

Online content

1. Novoselov, K. S. et al. Two-dimensional gas of massless Dirac fermions in graphene. *Nature* **438**, 197–200 (2005).
2. Castro Neto, A. H., Guinea, F., Peres, N. M. R., Novoselov, K. S. & Geim, A. K. The electronic properties of graphene. *Rev. Mod. Phys.* **81**, 109–162 (2009).
3. Das Sarma, S., Adam, S., Hwang, E. H. & Rossi, E. Electronic transport in two-dimensional graphene. *Rev. Mod. Phys.* **83**, 407–470 (2011).
4. Mikhailov, S. A. Non-linear graphene optics for terahertz applications. *Microelectronics J.* **40**, 712–715 (2009).
5. Al-Naib, I., Sipe, J. E. & Dignam, M. M. High harmonic generation in undoped graphene: interplay of inter- and intraband dynamics. *Phys. Rev. B* **90**, 245423 (2014).
6. Al-Naib, I., Poschmann, M. & Dignam, M. M. Optimizing third-harmonic generation at terahertz frequencies in graphene. *Phys. Rev. B* **91**, 205407 (2015).
7. Boyd, R. W. *Nonlinear Optics* 3rd edn (Academic, New York, 2008).
8. Reyna, A. S. & de Araújo, C. B. High-order optical nonlinearities in plasmonic nanocomposites—a review. *Adv. Opt. Photonics* **9**, 720–724 (2017).
9. Reshef, O. et al. Beyond the perturbative description of the nonlinear optical response of low-index materials. *Opt. Lett.* **42**, 3225–3228 (2017).
10. Bowlan, P., Martinez-Moreno, E., Reimann, K., Elsaesser, T. & Woerner, M. Ultrafast terahertz response of multilayer graphene in the nonperturbative regime. *Phys. Rev. B* **89**, 041408 (2014).
11. Yoshikawa, N., Tamaya, T. & Tanaka, K. High-harmonic generation in graphene enhanced by elliptically polarized light excitation. *Science* **356**, 736–738 (2017).
12. Zaks, B., Liu, R. B. & Sherwin, M. S. Experimental observation of electron–hole recollisions. *Nature* **483**, 580–583 (2012).
13. Schubert, O. et al. Sub-cycle control of terahertz high-harmonic generation by dynamical Bloch oscillations. *Nat. Photon.* **8**, 119–123 (2014).
14. Mics, Z. et al. Thermodynamic picture of ultrafast charge transport in graphene. *Nat. Commun.* **6**, 7655 (2015).
15. Green, B. et al. High-field high-repetition-rate sources for the coherent THz control of matter. *Sci. Rep.* **6**, 22256 (2016).
16. Winnerl, S. et al. Ultrafast processes in graphene: from fundamental manybody interactions to device applications. *Ann. Phys.* **529**, 1700022 (2017).
17. Jadidi, M. M. et al. Nonlinear terahertz absorption of graphene plasmons. *Nano Lett.* **16**, 2734–2738 (2016).
18. Hafez, H. A. et al. Nonlinear terahertz field-induced carrier dynamics in photoexcited epitaxial monolayer graphene. *Phys. Rev. B* **91**, 035422 (2015).
19. Breusing, M. et al. Ultrafast nonequilibrium carrier dynamics in a single graphene layer. *Phys. Rev. B* **83**, 153410 (2011).
20. Gierz, I. et al. Snapshots of non-equilibrium Dirac carrier distributions in graphene. *Nat. Mater.* **12**, 1119–1124 (2013).
21. Gierz, I. et al. Tracking primary thermalization events in graphene with photoemission at extreme time scales. *Phys. Rev. Lett.* **115**, 086803 (2015).
22. Winzer, T. & Malić, E. Impact of Auger processes on carrier dynamics in graphene. *Phys. Rev. B* **85**, 241404 (2012).
23. Song, J. C. W., Tielrooij, K. J., Koppens, F. H. L. & Levitov, L. S. Photoexcited carrier dynamics and impact-excitation cascade in graphene. *Phys. Rev. B* **87**, 155429 (2013).
24. Tomadin, A., Brida, D., Cerullo, G., Ferrari, A. C. & Polini, M. Nonequilibrium dynamics of photoexcited electrons in graphene: collinear scattering, Auger processes, and the impact of screening. *Phys. Rev. B* **88**, 035430 (2013).
25. Winnerl, S. et al. Carrier relaxation in epitaxial graphene photoexcited near the Dirac point. *Phys. Rev. Lett.* **107**, 237401 (2011).
26. Hwang, H. Y. et al. Nonlinear THz conductivity dynamics in p-type CVD-grown graphene. *J. Phys. Chem. B* **117**, 15819–15824 (2013).
27. Hendry, E., Hale, P. J., Moger, J., Savchenko, A. K. & Mikhailov, S. A. Coherent nonlinear optical response of graphene. *Phys. Rev. Lett.* **105**, 097401 (2010).
28. Hong, S. et al. Optical third-harmonic generation in graphene. *Phys. Rev. X* **3**, 021014 (2013).
29. Kumar, N. et al. Third harmonic generation in graphene and few-layer graphite films. *Phys. Rev. B* **87**, 121406 (2013).
30. Cheng, J. L., Vermeulen, N. & Sipe, J. E. Third-order nonlinearity of graphene: effects of phenomenological relaxation and finite temperature. *Phys. Rev. B* **91**, 235320 (2015).
31. König-Otto, J. C. et al. Four-wave mixing in Landau-quantized graphene. *Nano Lett.* **17**, 2184–2188 (2017).
32. Schwierz, F. Graphene transistors: status, prospects, and problems. *Proc. IEEE* **101**, 1567–1584 (2013).
33. Wehling, T. O., Black-Schaffer, A. M. & Balatsky, A. V. Dirac materials. *Adv. Phys.* **63**, 1–76 (2014).

METHODS

Basic experimental set-up. The experiments were performed at the TELBE THz facility, which provides tunable, narrow-band (bandwidth of 20%, FWHM), spectrally dense THz pulses in the frequency range between 0.1 THz and 1.2 THz with adjustable repetition rates up to the few 100-kHz regime. The multicycle THz pulses are generated in an undulator through the process of superradiance from ultra-short relativistic electron bunches accelerated and compressed in a quasi-continuous-wave superconducting radiofrequency accelerator[15]. In the standard mode of operation, a thermionic injector serves as the electron source and was used in most experiments. A recent upgrade now also allows the use of a specially developed photoinjector that provides higher electron bunch charges. This was used to perform the experiments at 0.3 THz central frequency, in particular enabling the observation of the seventh THz harmonic.

In these specific experiments, linearly polarized THz pulses with central frequencies 0.3 THz, 0.37 THz and 0.68 THz were used separately as input fundamental driving field. The input THz beam was focused on the graphene sample at normal incidence, and the transmitted (that is, re-emitted) THz waves were detected behind the sample (see Extended Data Fig. 1). All measurements were carried out at room temperature and under ambient atmosphere. The higher harmonic background was suppressed by appropriate shaping of the longitudinal electron bunch form and by additional narrow bandpass filters[34] before the sample, creating highly monochromatic pump fields with a bandwidth of roughly 10% (FWHM) (Extended Data Fig. 2). On transmission through the sample, the THz signal containing the remainder of the fundamental field, as well as the generated harmonics, was again sent through a set of bandpass filters with the transmission band centred at the generated harmonic to be detected. The resulting THz field was measured directly in the time domain by free-space electro-optic sampling (FEOS) in a 1.9-mm-thick ZnTe crystal[35], with the peak THz field strength not exceeding about 0.6 kV cm^{-1}. For FEOS THz detection, we used gating pulses of 100 fs duration, central wavelength 805 nm, from a commercial Ti:sapphire laser system (https://cohrcdn.azureedge.net/assets/pdf/RegA-Data-Sheet.pdf), which is synchronized and timed to the TELBE source[15]. The uncertainty in the timing between the THz pulses generated by the superradiant THz source and the probe laser pulses was less than 30 fs (FWHM)[36]. The specific choice of the 1.9-mm-thick ZnTe crystal enables sensitive THz field sampling only in the frequency range below 2.4 THz, which motivated our choice of the fundamental frequencies of $f = 0.68$ THz, $f = 0.37$ THz and $f = 0.3$ THz for harmonic generation at $3f = 2.04$ THz, $5f = 1.85$ THz and $7f = 2.1$ THz, respectively.

To achieve the optimal dynamic range required for measuring the field dependence of these different harmonics shown in Fig. 3a of the main text, specifically chosen bandpass filter combinations were used in the individual experimental configurations described in more detail later. Combined with the advanced pulse-resolved data acquisition scheme[36], dynamic ranges of better than 10^3 in the time-domain detection of the seventh and third harmonic fields, and 10^9 in the case of the fifth harmonic measurement, were achieved.

Pulse-resolved determination of THz intensities and fields. Depending on the tuning of the TELBE THz source, intensities can fluctuate between 10% and 50% with respect to the average value. The intensity of each THz pulse is recorded using a fast pyro detector with a bandwidth of 1 MHz in front of the first bandpass filter (see Extended Data Fig. 1). The THz pulses are thereafter grouped and evaluated in separate ranges around a certain pyro detector level. The width of these ranges defines the error bar in the pump fields in Fig. 3a. The absolute values for the intensity and the corresponding THz field are derived from a careful cross-calibration carried out before the experiment. For this, the intensity seen by the pyro detector was compared to that of the FEOS measurement at different pyro detector levels. The THz intensity was dimmed in front of the pyro detector and in front of the ZnTe crystal to avoid nonlinearities in both detection schemes. The peak fields at the sample position were determined from a combination of the beam profile, as measured by a commercial pyroelectric camera of the type Ophir Pyrocam III (https://www.ophiropt.com/laser-measurement/beam-profilers/products/Beam-Profiling/Camera-Profiling-with-BeamGage/Pyrocam-IIIHR), the THz pulse shape and intensity, as measured by the combination of FEOS and pyro detector, and the THz power, as determined by a commercial calibrated THz power-meter of the type Ophir 3A-P-THz (https://www.ophiropt.com/laser-measurement/laser-power-energy-meters/products/Laser-Thermal-Power-Sensors/High-Sensitivity-Thermal-Laser-Sensors/3A-P-THz)[37,38].

Simultaneous detection of the third, fifth and seventh harmonic. In this experiment, a fundamental frequency of 0.3 THz was chosen for generation and detection of the seventh harmonic at 2.1 THz. The repetition rate of the TELBE THz source was 100 kHz; the femtosecond laser had a repetition rate of 200 kHz. The particular configuration of bandpass filters, as shown in Extended Data Fig. 3, allowed not only the detection of the seventh harmonic but also simultaneous observation of the third and fifth harmonics at 0.9 THz and 1.5 THz (see Fig. 1). Two 0.3-THz bandpass filters were used to suppress the harmonic background of the undulator,

leading to a maximum field strength of 85 kV cm^{-1} at the sample. The resulting suppression factor in intensity is 10^{-8} for the third, 10^{-6} for the fifth and 10^{-4} for the seventh harmonic. The filtered THz beam was focused on the sample by an off-axis parabolic mirror in combination with an additional Teflon lens, which yielded a THz spot size of 560 μm (FWHM). A 2.1-THz bandpass filter was used behind the sample to enable optimal sensitivity for the seventh harmonic in the FEOS measurement, while still allowing a detectable portion of the lower harmonics and the fundamental to pass through.

The as-measured higher harmonic generation (HHG) spectrum from graphene is shown in Extended Data Fig. 4 (red curve). It clearly shows the fundamental and harmonics up to the seventh order. The raw signal originating from the bare SiO$_2$ substrate as a reference is shown in black. To determine the corresponding electric fields quantitatively, the transmission function of the 2.1-THz filter and the frequency-dependent sensitivity of the ZnTe detection crystal must be included. The former has been measured and is displayed in Extended Data Fig. 4 as the grey curve, showing the substantial suppression of frequencies below 1.9 THz. The spectra presented in Fig. 1b were obtained by deconvoluting the response functions of both the ZnTe detection crystal and the 2.1-THz filter from the measured FEOS signals (see discussion in the next section on reconstructing the harmonic fields from the measured FEOS signals and Extended Data Fig. 9). In order not to overly amplify the noise above 2.2 THz in the graphene sample and reference spectra, the ZnTe sensitivity curve was assumed to be flat for values above 2.2 THz in this case. This does not affect either the overall peak shape in Fig. 1 or the peak field values that were used to calculate the efficiencies of HHG (see Fig. 3a and Table 1).

Separate detection of the third and fifth harmonic at 2.04 THz and 1.85 THz. The repetition rate of the TELBE THz source was set to 101 kHz; the femtosecond laser used for FEOS detection had a repetition rate of 202 kHz. To explicitly measure and quantify (see Fig. 3a) the electric field strength of the third harmonic generation (THG) and fifth harmonic generation (FHG) signals, we chose the fundamental frequencies of 0.68 THz and 0.37 THz, respectively. Sets of narrow-bandpass filters[34] were tailored correspondingly. These filters suppress the higher harmonic background to less than 10^{-7} for 0.68 THz and to less than 10^{-11} for 0.37 THz in intensity. Thereby, we reached an optimal dynamic range in the FEOS detection of the harmonic field, despite the fact that the harmonic field is weaker than the fundamental field by a factor of 10^{-3} (THG) or 10^{-4} (FHG). Beam diameters (FWHM) on the sample surface were 1 mm for 0.68 THz and 0.6 mm for 0.37 THz. In the latter case, an additional Teflon lens was used to optimize the spot size.

In Extended Data Fig. 5a, we show a schematic of the beampath in the THG experiment. Here a single 1.93-THz bandpass filter[34] was introduced after the sample to attenuate the fundamental at 0.68 THz, while allowing transmission of the THG signal at 2.04 THz. The spectral transmission function of the 1.93-THz filter is shown in Extended Data Fig. 6a. Extended Data Fig. 6b shows the as-measured amplitude spectra of the detected FEOS signals: the reference (pump field transmitted through a bare SiO$_2$ substrate) and that from the sample (pump field transmitted through graphene on a SiO$_2$ substrate). The pump field contains a small spurious contribution at the THG frequency (black line in Extended Data Fig. 6b), which is, however, an order of magnitude smaller than the THG generated in graphene (red line in Extended Data Fig. 6b).

In the case of the THG experiment, the leaking field at the fundamental frequency $f = 0.68$ THz measured through the bare SiO$_2$ substrate (geometry as shown in Extended Data Fig. 5a) serves as a representative for the fundamental THz excitation field in Extended Data Fig. 10 and was used as a reference input pulse in the theoretical model.

In the FHG experiment, we used the beampath as schematically shown in Extended Data Fig. 5b. To ensure greater sensitivity for the detection of the fifth harmonic field, the number of bandpass filters before and after the sample was doubled for all fields except for the three highest field values shown in Fig. 3a, for which the 0.4-THz filter was removed. Extended Data Fig. 7 shows the as-measured amplitude spectra of the detected reference and sample FEOS signals. The transmission at the fundamental frequency is strongly suppressed, and no spurious contribution of the pump field at the FHG frequency is observed.

Because the signal of the 0.37-THz fundamental in this configuration was small, it was (in contrast to the THG experiment) not suitable to derive the waveform of the fundamental THz pulse from the leaking fundamental. Instead, the waveform was measured with an additional experimental configuration shown in Extended Data Fig. 5c. This waveform was also used as a reference input pulse for the theoretical calculation of the nonlinear response of graphene.

Reconstruction of the harmonic fields from the measured FEOS signals. The complex-valued (that is, containing both amplitude and phase) field transmission functions of all optical elements in the THz beampath of our experiments (sample substrate, bandpass filters), as well as the FEOS detector (THz Fresnel insertion losses, and the frequency-dependent acceptance function of the FEOS ZnTe crystal which is described in refs [39,40]) have been characterized, as summarized below.

As a result, rigorous reconstruction of the measured FEOS signals back to the actual, calibrated THz electric field transients at all frequencies of interest (fundamental and higher harmonics) was possible. Our reconstruction from the FEOS signals back to the actual fields follows the same general protocol reported in ref. [41], while taking into account all elements in the THz beampath. Here we exemplify the field reconstruction from the measured EOS using the THz THG experiment with $f = 0.68$ THz $\rightarrow 3f = 2.04$ THz.

Extended Data Fig. 6a shows the amplitude transmission spectrum of the 1.93 THz bandpass filter, while Extended Data Fig. 8 shows the phase and thereby time difference added to the signals at all frequencies of interest owing to the propagation through this optical element. A THz time-domain spectroscopy measurement of the SiO₂ substrate yielded values of frequency-dependent power absorption coefficient of 7.6 cm⁻¹ (2.04 THz), 6.6 cm⁻¹ (1.85 THz), 2.3 cm⁻¹ (0.68 THz) and 1.3 cm⁻¹ (0.37 THz), and a spectrally flat refractive index of 1.98, in good agreement with the literature[42].

In Extended Data Fig. 9a, we show the frequency-dependent transmission response function (amplitude transmission and phase shift) of the bare SiO₂ substrate, while in Extended Data Fig. 9b we show the acceptance function (amplitude and phase shift)[39] of our FEOS unit: 1.9-mm-thick ZnTe crystal, gated by the 100-fs pulses at 805-nm central wavelength.

Taking all the above elements used in the THz transmission and detection in our experiment, we are now able to rigorously reconstruct the as-measured THz FEOS signals back into the actual THz-field waveforms[41], as shown in Extended Data Fig. 10 (example of THG measurement with $f = 0.68$ THz $\rightarrow 3f = 2.04$ THz).

Extended Data Fig. 10a shows the measured FEOS signals transmitted through the bare substrate (black pulse), through the graphene/substrate sample (red pulse), both normalized to the peak of the substrate pulse, and the difference between the two normalized FEOS signals (blue pulse). The difference pulse (the blue one) clearly shows oscillations at the THG frequency of 2.04 THz. Extended Data Fig. 10b shows the corresponding reconstructed fields (the fields at the point just after the graphene–substrate interface) after compensating for the field losses and deconvoluting the response functions, described above, of the optical elements after the graphene–substrate interface. We note that deconvoluting the phase shift induced by these optical elements after the graphene film from the FEOS signals in Extended Data Fig. 10a results in a time-shift of about 17.8 ps to the reconstructed fields in Extended Data Fig. 10b. Further, in the reconstructed fields in Extended Data Fig. 10b, the fundamental field is upscaled to its original values before the bandpass filter attenuation after the sample, and in turn dominates over the THG. Thus, the oscillation at the THG frequency included in the difference field pulse (blue pulse) in Extended Data Fig. 10b is now less pronounced than that in Extended Data Fig. 10a. Now, if we spectrally remove the fundamental signal at 0.68 THz from the field difference pulse shown in Extended Data Fig. 10b, we arrive at the THG field waveform (Extended Data Fig. 10c).

Sample preparation and characterization. Our sample is a typical CVD-grown monolayer graphene transferred onto a fused silica substrate[14,43,44]. The graphene quality was tested by Raman spectroscopy, which showed a single layer identity with a large-scale homogeneity (see Extended Data Fig. 11a for the Raman spectra of the sample). The characteristic graphene 2D and G peaks[45] are observed at 2703 cm⁻¹ and 1591 cm⁻¹, respectively. The Gaussian shape of the 2D band with FWHM of about 47 cm⁻¹, along with the relative ratio of the 2D peak to the G peak, denotes single layer identity of the graphene sample. The very weak D band at 1,300 cm⁻¹ is indicative of a low defect density.

The linear conductivity of our graphene sample was characterized by THz time-domain spectroscopy using a ZnTe crystal as a THz emitter pumped by 800-nm laser pulses with a pulse width of 40 fs and a repetition rate of 1 kHz. The experimental data revealed Drude-type conductivity[14,46–49], providing the Fermi level energy of 170 meV and electron momentum scattering time of 47 fs (see Extended Data Fig. 11b for the linear THz characterization of the sample).

We note here that our graphene sample is, in fact, p-type, as is typical for CVD-grown material deposited on fused SiO₂ substrate in the presence of ambient atmosphere (see for example ref. [50]). However, owing to the symmetry of the band structure for Dirac electrons and holes in graphene, for simplicity we depict the Fermi level in the conduction rather than in the valence band.

Calculations. The (nonlinear) complex-valued THz field transmission from the free space through graphene into the substrate is described by the Tinkham equation[51]

$$\tilde{E}_t(\omega) = \frac{2}{n_s + 1 + Z_0\tilde{\sigma}(\omega)}\tilde{E}_{in}(\omega) \tag{1}$$

where n_s is the refractive index of the substrate, Z_0 is the free-space impedance and $\tilde{\sigma}(\omega)$ is the complex THz conductivity of the conductive film, and $\tilde{E}_{in}(\omega)$ is the complex-valued THz incident field. The conductivity $\tilde{\sigma}(\omega)$ is nonlinear on the driving THz field[14,18,25,26,52,53]; see also the discussion below.

The intraband conductivity of conduction-band electrons of graphene at THz frequencies $\tilde{\sigma}(\omega)$ can generally be described by the solution of the Boltzmann equation[3,14,54]:

$$\tilde{\sigma}(\omega) = -\frac{e^2 v_F^2}{2}\int_0^\infty D(E)\frac{\tau(E)}{1 - i\omega\tau(E)}\frac{\partial f_{FD}(E,\mu,T_e)}{\partial E}dE \tag{2}$$

where $v_F = 1 \times 10^6$ m s⁻¹ is the Fermi velocity of the relativistic Dirac fermions in graphene, $\tau(E)$ is the energy-dependent electron scattering time, $D(E) = 2|E|/\pi(\hbar v_F)^2$ is the density of states of the graphene energy bands, and $f_{FD}(E,\mu,T_e) = \{\exp[(E - \mu)/(k_B T_e)] + 1\}^{-1}$ is the Fermi–Dirac distribution function for a chemical potential μ and electron temperature T_e.

The dominating electron momentum scattering mechanism in CVD-grown graphene deposited on fused silica substrate is through Coulomb interactions with charged impurities (long-range Coulomb scattering)[3,14,55–58], which is defined by linear dependence of scattering time on energy $\tau(E) = \gamma E$ (see also ref. [59]). The proportionality constant $\gamma = \tau_0/E_F = 47$ fs/(170 meV) can be obtained from the linear response described above (see also ref. [14] and Extended Data Fig. 11b). In terms of the THz-field-induced heat density ΔQ, one can express $\tau(\Delta Q) = \gamma(E_F + \Delta Q/N_c) = \tau_0 + \gamma\Delta Q/N_c$, where $N_c = \int_0^\infty D(E)f_{FD}(E,\mu,T_e)dE$.

To compute the time-dependent THz-field-induced heat ΔQ accumulated in the electronic system of graphene during the (nonlinear) interaction with the driving THz wave, split-step time-domain calculations, as common in nonlinear optics, must be performed (see for example ref. [60]). For this, the inverse Fourier transforms of equation (1) with the conductivity $\tilde{\sigma}(\omega)$ described by equation (2) must be taken at every time step during numerical propagation. To speed up the calculations, a linear parameterization of equation (2) has been used, under the conditions of energy conservation (all absorbed THz energy adds to ΔQ) and free-carrier density conservation ($N_c = \int_0^\infty D(E)f_{FD}(E,T_e)dE = $ constant), yielding the following expression

$$\tilde{\sigma}(\omega) \approx \frac{(ev_F)^2\gamma N_c}{1 - i\omega\tau(\Delta Q)} \tag{3}$$

Now, the time-domain expression of the THz field transmission of graphene, by taking the inverse Fourier transform of equation (1) with the conductivity $\tilde{\sigma}(\omega)$ described by equation (3), results in a time-dependent response function

$$T(t) = \frac{2\delta(t)}{n_s + 1} - \frac{2Z_0(ev_F)^2\gamma N_c}{[\tau_0 + \gamma\Delta Q(t)/N_c](n_s + 1)^2}$$
$$\times\exp\left\{-\frac{Z_0(ev_F)^2\gamma N_c + n_s + 1}{[\tau_0 + \gamma\Delta Q(t)/N_c](n_s + 1)}t\right\} \tag{4}$$

where $\delta(t)$ is the Dirac delta function. The convolution of this function with the temporal THz driving field $E_{in}(t)$ yields the corresponding temporal field transmitted through the graphene film into the SiO₂ substrate:

$$E_t(t) = T(t) * E_{in}(t) \tag{5}$$

where the asterisk denotes the convolution.

To accommodate for the electron cooling due to phonon emission, we use the following cooling rate as directly measured in ref. [20]

$$R(t) = 0.001\exp\left(-\frac{t}{\tau_1}\right) + 0.46\exp\left(-\frac{t}{\tau_2}\right) + 0.539\exp\left(-\frac{t}{\tau_3}\right) \tag{6}$$

with time constants $\tau_1 = 13$ fs, $\tau_2 = 80$ fs and $\tau_3 = 0.86$ ps. This relaxation process leads to a recovery towards the initial linear conductivity of the graphene after the incident THz pulse ceases. The calculation of the THz-induced heat is thus based on the following convolution:

$$\Delta Q(t) = \frac{1}{2}\varepsilon_0 cR(t) * \{E_{in}^2(t) - n_s E_t^2(t) - [E_t(t) - E_{in}(t)]^2\} \tag{7}$$

where ε_0 is the vacuum permittivity.

As a result, the time-dependent induced electronic heat given by equation (7) leads to the temporal modulation of conductivity and results in the nonlinear response function of graphene described by equation (4), which in turn leads to harmonic generation.

The nonlinear THz refractive index of graphene. The dielectric function of the graphene film can be expressed by[61,62]

$$\varepsilon_r = \varepsilon_\infty + \frac{i\tilde{\sigma}}{d\omega\varepsilon_0} \tag{8}$$

where $d = 0.3$ nm is the thickness of the graphene film and $\varepsilon_\infty \approx 1$ (refs [61,62]). We calculate the real part of the refractive index using $n = \text{Re}\{\sqrt{\varepsilon_r}\}$. Substituting the

linear Drude conductivity shown in Extended Data Fig. 11b into equation (8), we first obtain the linear (field-independent) refractive index (for fields less than $1\,\mathrm{kV\,cm^{-1}}$). When the graphene film interacts with higher fields, the conductivity decreases as explained above, leading to a reduction in the refractive index (Extended Data Fig. 12). In Extended Data Fig. 12a, we show the calculated field-dependent THz index when the graphene film is pumped by THz fields at a fundamental frequency of 0.3 THz. In Extended Data Fig. 12b, we show the THz field dependence of the nonlinear refractive index at the harmonics $3f = 2.04\,\mathrm{THz}$ generated by the $f = 0.68\,\mathrm{THz}$ pump, $5f = 1.85\,\mathrm{THz}$ generated by the $f = 0.37\,\mathrm{THz}$ pump, and $7f = 2.1\,\mathrm{THz}$ generated by the $f = 0.3\,\mathrm{THz}$ pump. From this field dependence of the refractive index, we estimated the third-, fifth- and seventh-order susceptibilities $\chi^{(3)}$, $\chi^{(5)}$ and $\chi^{(7)}$, respectively, as explained in the next section.

Extraction of nonlinear coefficients of graphene. The conservative, low-boundary estimate of the third-, fifth- and seventh-order THz nonlinear optical coefficients of graphene, based on the experimentally measured field conversion efficiencies in small-signal regime (power-law fits to the data and the results of thermodynamic model in Fig. 3a) is done as follows. Ignoring both the pump field depletion (given approximately 90% field transmission through graphene in the most absorptive limit of small driving THz fields), and the phase mismatch in $f \rightarrow mf$ conversion processes (negligible within one atomic layer), the conversion from the pump to the harmonic field is defined as $|E_{mf}| = \gamma L |E_f|^m$ with $\gamma = k_m[\pi f/(cn_{mf})]\chi^{(m)}_{\mathrm{eff}}$ (refs [7,63]). Here $m = (3,5,7)$ is the harmonic order; E_f and E_{mf} are peak electric field strengths of the incident fundamental and generated mth harmonic field, respectively; $k_m = (3/4, 5/16, 7/64)$ is a numerical coefficient for harmonics $m = 3$, 5 and 7, respectively; $L = 0.3\,\mathrm{nm}$ is the thickness of graphene layer[64]; c is the speed of light in vacuum; and n_{3f}, n_{5f} and n_{7f} represent the refractive indices of graphene at the harmonic frequencies, which at the target harmonic frequency around 2 THz is chosen to be about 10 (see below). From the measured THG with $f = 0.68\,\mathrm{THz} \rightarrow 3f = 2.04\,\mathrm{THz}$, the field conversion coefficient of $\gamma L = |E_{3f}|/|E_f|^3 = 1.79 \times 10^{-16}\,\mathrm{m^2\,V^{-2}}$, and an estimate of the effective third-order THz nonlinear susceptibility of graphene is $\chi^{(3)}_{\mathrm{eff}} \approx 1.7 \times 10^{-9}\,\mathrm{m^2\,V^{-2}}$. For the measured FHG with $f = 0.37\,\mathrm{THz} \rightarrow 5f = 1.85\,\mathrm{THz}$, the field conversion coefficient $\gamma L = |E_{5f}|/|E_f|^5 = 2.68 \times 10^{-30}\,\mathrm{m^4\,V^{-4}}$ and the effective fifth-order THz nonlinear susceptibility of graphene is estimated as $\chi^{(5)}_{\mathrm{eff}} \approx 1.2 \times 10^{-22}\,\mathrm{m^4\,V^{-4}}$. In the same fashion, for the seventh harmonic generation (7HG) process with $f = 0.3\,\mathrm{THz} \rightarrow 7f = 2.1\,\mathrm{THz}$, the field conversion coefficient $\gamma L = |E_{7f}|/|E_f|^7 = 1.8 \times 10^{-46}\,\mathrm{m^6\,V^{-6}}$ and the estimate of the effective seventh-order THz nonlinear susceptibility of graphene is $\chi^{(7)}_{\mathrm{eff}} \approx 1.74 \times 10^{-38}\,\mathrm{m^6\,V^{-6}}$.

We note that the value for the refractive index of graphene of $n_{3f,5f,7f} \approx 10$ (at the frequency around 2 THz, and at high electron temperature) used in our calculations is a conservative order-of-magnitude estimate, as the actual values can be as high as $n \approx 20$–80 (Extended Data Fig. 12b), which will increase the values of the retrieved nonlinear coefficients of graphene even further.

Limits of the thermodynamic model of THz response of graphene in terms of driving THz field strength. The electron response, following the heating–cooling dynamics of electron population as described in this paper, will dominate the THz intraband nonlinearity of graphene until the regime of coherent Bloch oscillations will be reached. In this regime (see, for example, refs [13,65]), the conduction band electron reaches the Brillouin zone boundary in the time much faster than the typical electron momentum scattering (Drude) time, providing for the coherent nonlinear current (Bloch) oscillations in the k space of the Brillouin zone between the $k = \pi/a$ and $-k = -\pi/a$ points, where a is the lattice constant. We use the acceleration theorem $\mathrm{d}k/\mathrm{d}t = -eE/\hbar$, which can be further simplified to $\Delta k/\tau = -eE/\hbar$, where $\Delta k = \pi/a$ is the Brillouin zone half-width, $a = 0.14\,\mathrm{nm}$ is the lattice constant of graphene, and τ is the electron momentum relaxation time. For the typical electron momentum relaxation time in the range $\tau = 10$–100 fs (see, for example, ref. [3]) we arrive at the electric field strength range $E = 1$–$10\,\mathrm{MV\,cm^{-1}}$. This field strength thus sets the estimated upper validity limit for our model.

Data and code availability. The datasets generated and analysed during this study, and the corresponding computer codes, are available from the corresponding authors on reasonable request.

34. Kuznetsov, S. A., Astafyev, M. A., Gelfand, A. V. & Arzhannikov, A. V. Microstructured frequency selective quasi-optical components for submillimeter-wave applications. In *44th European Microwave Conference (EuMC)*, 881 (IEEE, Rome, 2014).
35. Wu, Q., Litz, M. & Zhang, X. C. Broadband detection capability of ZnTe electro-optic field detectors. *Appl. Phys. Lett.* **68**, 2924–2926 (1996).
36. Kovalev, S. et al. Probing ultra-fast processes with high dynamic range at 4th-generation light sources: arrival time and intensity binning at unprecedented repetition rates. *Struct. Dyn.* **4**, 024301 (2017).
37. Steiger, A., Kehrt, M., Monte, C. & Müller, R. Traceable terahertz power measurement from 1 THz to 5 THz. *Opt. Express* **21**, 14466–14473 (2013).
38. Müller, R. et al. Novel detectors for traceable THz power measurements. *J. Infrared Millim. Terahertz Waves* **35**, 659–670 (2014).
39. Gallot, G., Zhang, J., Mcgowan, R. W., Jeon, T. & Grischkowsky, D. Measurements of the THz absorption and dispersion of ZnTe and their relevance to the electro-optic detection of THz radiation. *Appl. Phys. Lett.* **74**, 3450 (1999).
40. Wu, Q. & Zhang, X. Ultrafast electro-optic field sensors. *Appl. Phys. Lett.* **68**, 1604 (1996).
41. Kampfrath, T. et al. Terahertz spin current pulses controlled by magnetic heterostructures. *Nat. Nanotech.* **8**, 256–260 (2013).
42. Parker, T. J. & Ford, J. E. The optical constants of pure far-infrared. *Infrared Phys.* **18**, 215–219 (1978).
43. Li, X. et al. Large-area synthesis of high-quality and uniform graphene films on copper foils. *Science* **324**, 1312–1314 (2009).
44. Hao, Y. et al. The role of surface oxygen in the growth of large single-crystal graphene on copper. *Science* **342**, 720–723 (2013).
45. Ferrari, A. C. et al. Raman spectrum of graphene and graphene layers. *Phys. Rev. Lett.* **97**, 187401 (2006).
46. Mak, K. F., Ju, L., Wang, F. & Heinz, T. F. Optical spectroscopy of graphene: from the far infrared to the ultraviolet. *Solid State Commun.* **152**, 1341–1349 (2012).
47. Jnawali, G., Rao, Y., Yan, H. & Heinz, T. F. Observation of a transient decrease in terahertz conductivity of single-layer graphene induced by ultrafast optical excitation. *Nano Lett.* **13**, 524–530 (2013).
48. Dawlaty, J. M. et al. Measurement of the optical absorption spectra of epitaxial graphene from terahertz to visible. *Appl. Phys. Lett.* **93**, 131905 (2008).
49. Frenzel, A. J. et al. Observation of suppressed terahertz absorption in photoexcited graphene. *Appl. Phys. Lett.* **102**, 113111 (2013).
50. Wang, H. I. et al. Reversible photochemical control of doping levels in supported graphene. *J. Phys. Chem. C* **121**, 4083–4091 (2017).
51. Glover, R. E. & Tinkham, M. Conductivity of superconducting films for photon energies between 0.3 and 40 kT_c. *Phys. Rev.* **108**, 243–256 (1957).
52. Suess, R. J. et al. Role of transient reflection in graphene nonlinear infrared optics. *ACS Photonics* **3**, 1069–1075 (2016).
53. Hafez, H. A. et al. Intense terahertz field effects on photoexcited carrier dynamics in gated graphene. *Appl. Phys. Lett.* **107**, 251903 (2015).
54. Marder, M. P. in *Condensed Matter Physics*, 483–493 (Wiley, Hoboken, NJ, 2010).
55. Tielrooij, K. J. et al. Photoexcitation cascade and multiple hot-carrier generation in graphene. *Nat. Phys.* **9**, 248–252 (2013).
56. Hwang, E. H. & Das Sarma, S. Acoustic phonon scattering limited carrier mobility in two-dimensional extrinsic graphene. *Phys. Rev. B* **77**, 115449 (2008).
57. Hwang, E. H. & Das Sarma, S. Screening-induced temperature-dependent transport in two-dimensional graphene. *Phys. Rev. B* **79**, 165404 (2009).
58. Perebeinos, V. & Avouris, P. Inelastic scattering and current saturation in graphene. *Phys. Rev. B* **81**, 195442 (2010).
59. Lundstrom, M. *Fundamentals of Carrier Transport* 2nd edn (Cambridge Univ. Press, New York, 2000).
60. Liu, X., Laegsgaard, J. & Turchinovich, D. Self-stabilization of a mode-locked femtosecond fiber laser using a photonic bandgap fiber. *Opt. Lett.* **35**, 913–915 (2010).
61. Lin, I. et al. Terahertz optical properties of multilayer graphene: experimental observation of strong dependence on stacking arrangements and misorientation angles. *Phys. Rev. B* **86**, 235446 (2012).
62. Gosciniak, J. & Tan, D. T. H. Theoretical investigation of graphene-based photonic modulators. *Sci. Rep.* **3**, 1897 (2013).
63. Saltiel, S. M., Sukhorukov, A. A. & Kivshar, Y. S. in *Progress in Optics* Vol. 47 (ed. Wolf, E.) 1–73 (Elsevier, Amsterdam, 2005).
64. Shearer, C. J., Slattery, A. D., Stapleton, A. J., Shapter, J. G. & Gibson, C. T. Accurate thickness measurement of graphene. *Nanotechnology* **27**, 125704 (2016).
65. Hohenleutner, M. et al. Real-time observation of interfering crystal electrons in high-harmonic generation. *Nature* **523**, 572–575 (2015).
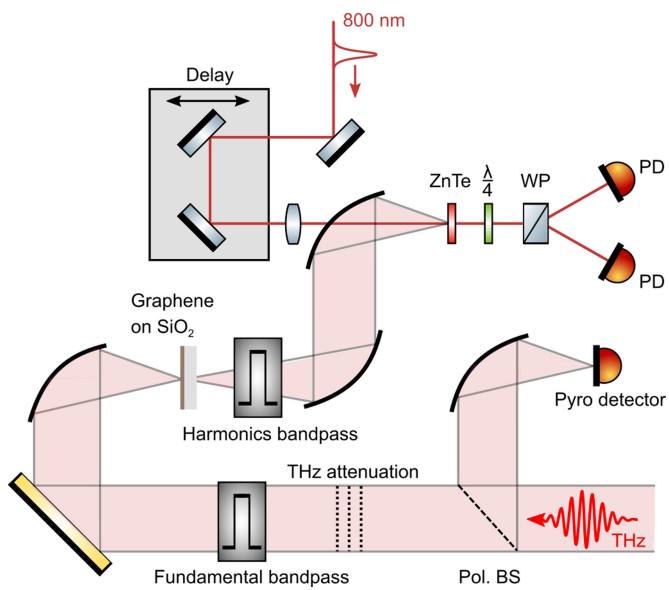
Extended Data Fig. 1 | Experimental set-up. Tunable multicycle THz pulses (red) from the undulator of the TELBE facility[2] are used to irradiate the graphene sample. 100-fs pulses from a Ti:sapphire laser system (brown) are used to probe the transmitted and emitted THz pulses by free-space electro-optic sampling. PD, photodiode; BS, beamsplitter; Pol., polarizer.
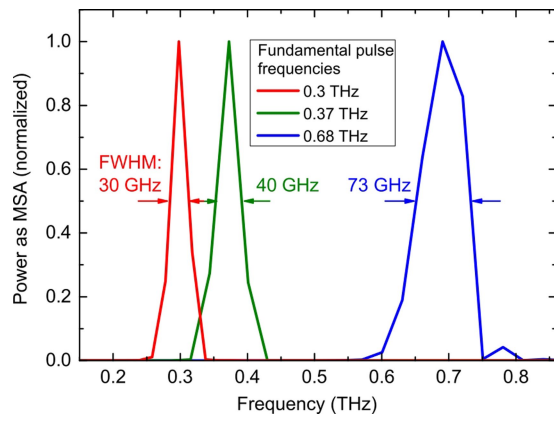
Extended Data Fig. 2 | Fundamental frequencies after bandpass filtering. The bandwidths were determined from Gaussian fits to the spectra. MSA, mean square amplitude.
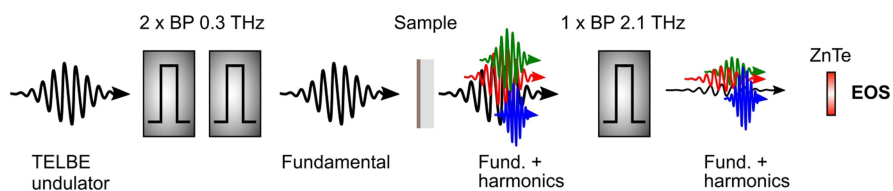
Extended Data Fig. 3 | Scheme of the set-up for detection of multiple harmonics up to the seventh order. Two 0.3-THz bandpass filters (BP) are used to suppress the undulator harmonic background. A single 2.1-THz bandpass filter after the sample attenuates the fundamental, third and fifth harmonics to an extent that they can still be detected by the EOS set-up.
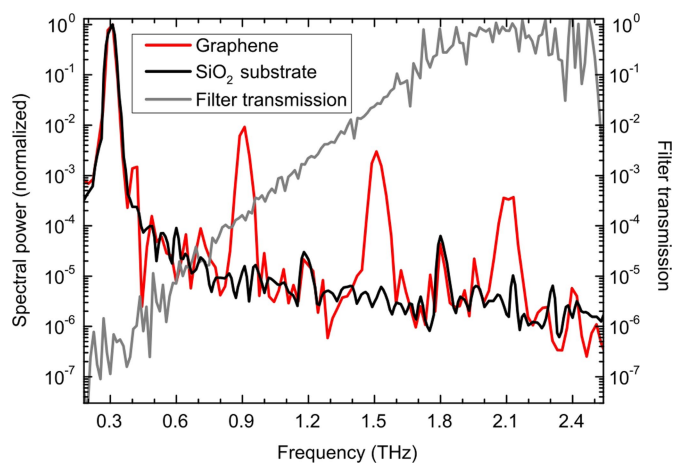
Extended Data Fig. 4 | HHG signal from graphene, reference signal from the SiO$_2$ substrate and filter function of the 2.1-THz bandpass. The red curve shows the as-measured HHG spectrum of the graphene sample. The black curve shows the reference spectrum taken from the bare SiO$_2$ substrate. The measured transmission function of the 2.1-THz bandpass filter is also shown (grey line).
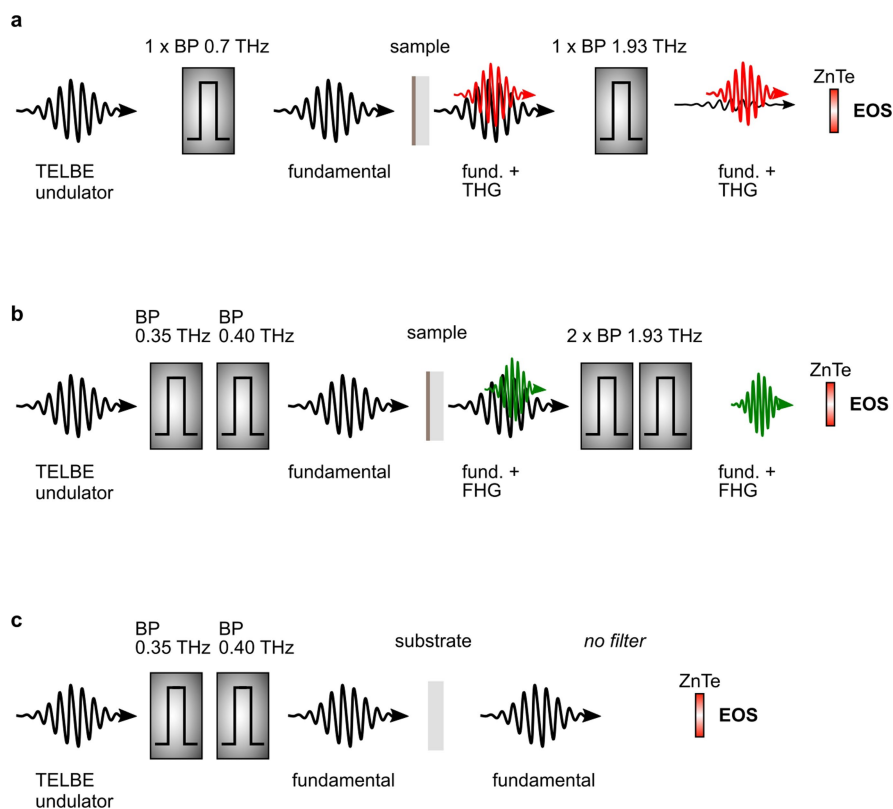
Extended Data Fig. 5 | Schemes of the experimental configurations to determine the electric fields of the fundamental, THG and FHG pulses. Measurements were performed with graphene/SiO$_2$ and with the bare SiO$_2$ substrate. **a**, Set-up for the THG experiment used to measure the fundamental and harmonic simultaneously. **b**, Set-up to measure the harmonic in the FHG experiment. Two filters were used before the sample and two after the sample, to optimize the signal-to-noise ratio. **c**, Set-up to determine the electric fields for the fundamental in the FHG experiment.

a

b
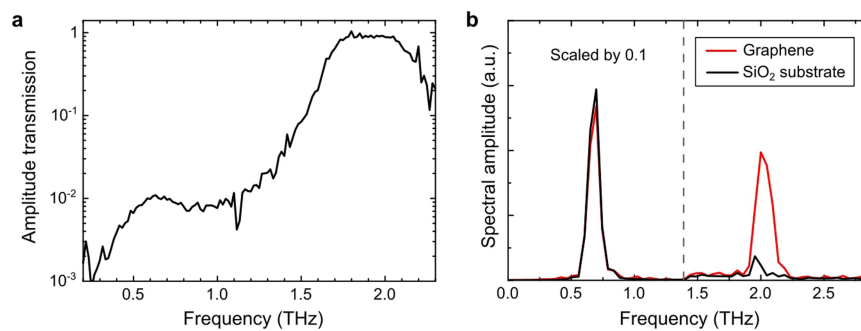
Extended Data Fig. 6 | Filter function of the 1.93-THz bandpass and raw spectra from the THG experiment. a, Amplitude transmission function of a single 1.93-THz bandpass filter. **b**, As-measured spectral amplitude in arbitrary units (a.u.), as determined from the bare SiO_2 substrate (black) and from the graphene sample (red). The incident THz peak field of the fundamental at 0.68 THz was 61 kV cm^{-1}.
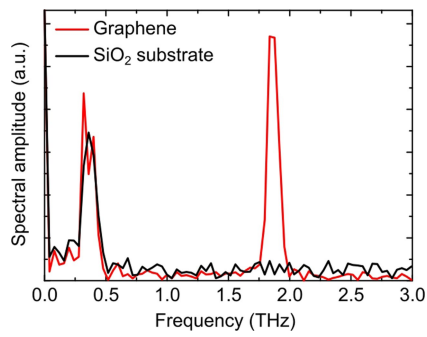
Extended Data Fig. 7 | Raw spectra from the FHG experiment.
These as-measured spectra show the spectral amplitude as determined from a measurement with the bare SiO_2 substrate as a reference and a measurement of the graphene sample. The incident THz peak field in the fundamental at 0.37 THz was 40 kV cm^{-1} when using two filters in the incident beam. Insignificant transmission at the fundamental frequency and no spurious background at the FHG frequency band is observed in the reference field measurement.
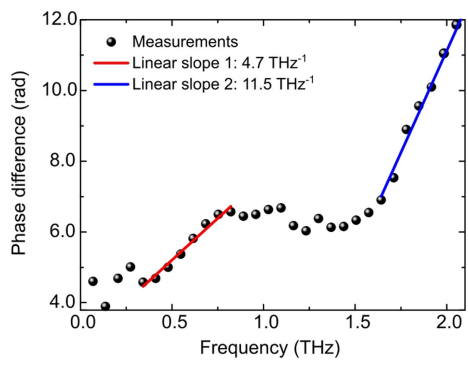
Extended Data Fig. 8 | Frequency-dependent phase difference induced by the 1.93-THz bandpass filter.
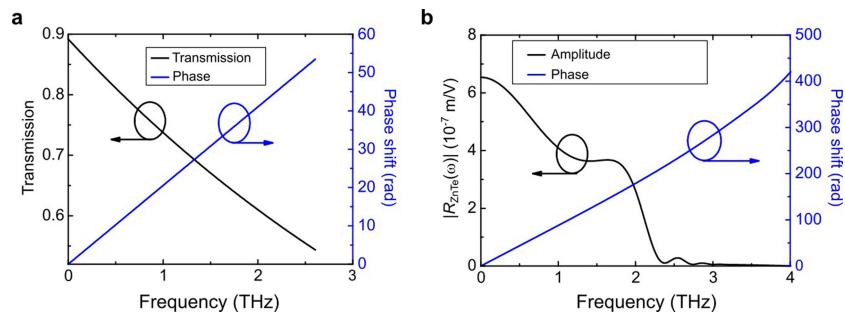
Extended Data Fig. 9 | The frequency-dependent response function.
a, The bare substrate described by the amplitude transmission (black line) and the substrate-induced phase shift (blue line). **b**, A simulated acceptance function of the 1.9-mm-thick ZnTe detection crystal; amplitude (black curve) and phase shift (blue curve). Arrows indicate relevant axis.
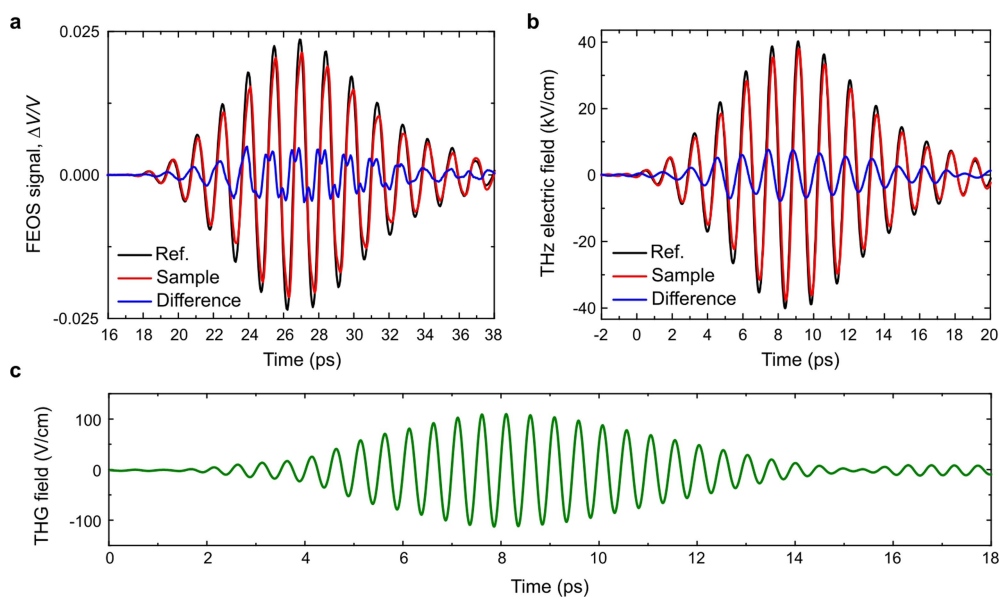
Extended Data Fig. 10 | Reconstruction of the harmonic fields from the measured FEOS signals. This is an example of THG measurement with $f = 0.68$ THz $\rightarrow 3f = 2.04$ THz. **a**, Measured FEOS signals (dimensionless). **b**, The corresponding fields transmitted through the incidence interface of the sample after deconvoluting the response functions of all the elements after the graphene film, including the 1.9-mm-thick ZnTe detection crystal, the 1.93-THz filter and the fused silica substrate from the FEOS signals in **a**. Black pulse is for the bare substrate, red for the graphene sample and blue for the difference. **c**, The pure THG field extracted from the blue field pulse in **b**.
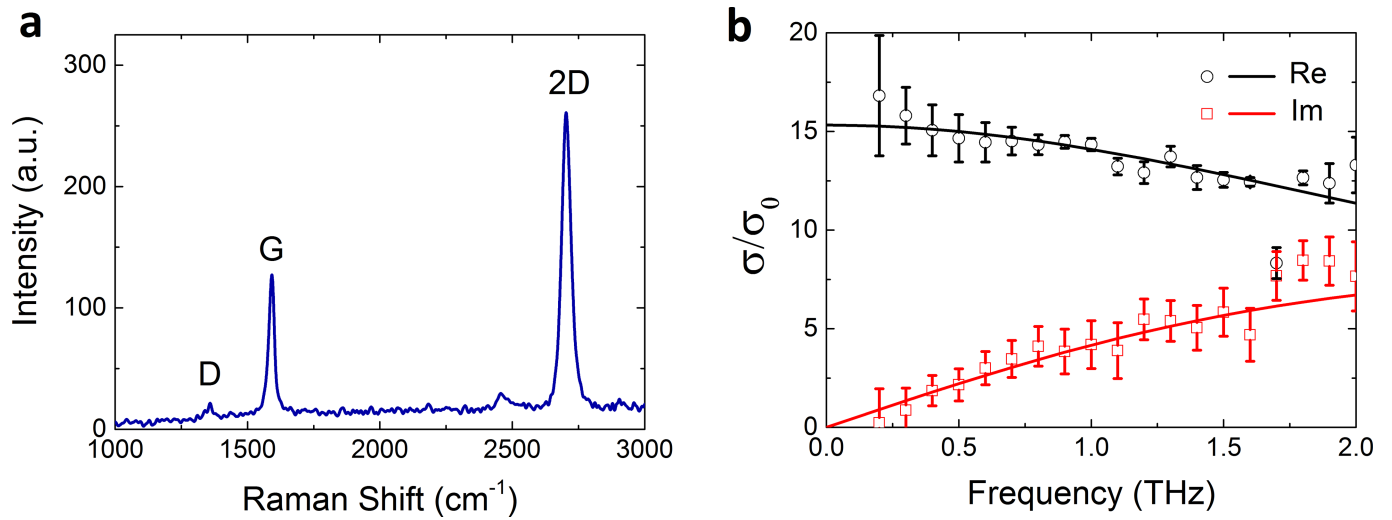
Extended Data Fig. 11 | Characterization of the graphene sample. **a**, Raman spectrum of the graphene sample. **b**, Linear conductivity, real and imaginary, of the graphene film normalized to the universal conductivity $\sigma_0 = e^2/(4\hbar)$. The symbols represent the experimental data; the solid lines represent the Drude fit with a Fermi level energy $E_F = 170$ meV (corresponding to a doping concentration $N_c = 2.1 \times 10^{12}$ cm^{-2}) and a scattering time $\tau_0 = 47$ fs as fitting parameters. The error bars are the standard deviation in the measurements.
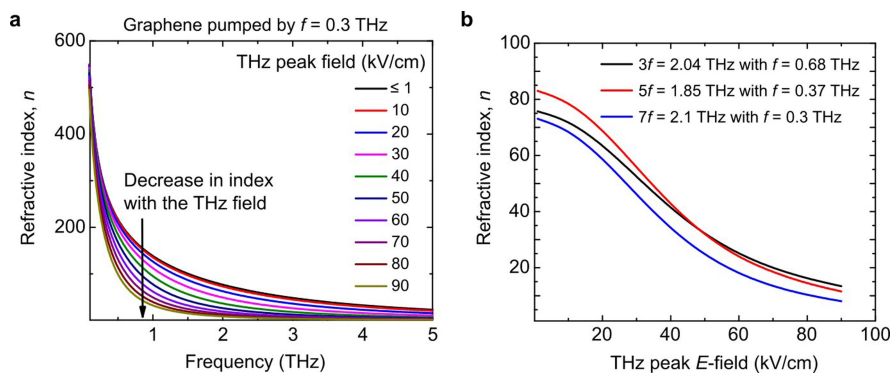
Extended Data Fig. 12 | The nonlinear (THz-field-dependent) refractive index of the graphene film. a, The THz refractive index of the graphene film as a function of frequency at various peak electric fields for the THz pump at 0.3 THz, showing reduction in the refractive index with both frequency and exciting field strength. **b**, The field dependence of the nonlinear THz refractive index at the harmonics $3f = 2.04$ THz generated by $1f = 0.68$ THz pump, $5f = 1.85$ THz generated by $1f = 0.37$ THz pump, and $7f = 2.1$ THz generated by $1f = 0.3$ THz pump.